

# Water clarity patterns in South Florida coastal waters and their linkages to synoptic-scale wind forcing

Douglas E Pirhalla<sup>1\*</sup>, Scott C Sheridan<sup>2</sup>, Cameron C Lee<sup>2</sup>, Brian B Barnes<sup>3</sup>, Varis Ransibrahmanakul<sup>1</sup>, Chuanmin Hu<sup>3</sup>

<sup>1</sup> National Oceanic and Atmospheric Administration, National Ocean Service, USA

<sup>2</sup> Kent State University, Department of Geography, USA

<sup>3</sup> University of South Florida, College of Marine Science, USA

<sup>4</sup> NOAA National Centers for Environmental Information, USA

**Abstract:** Temporal variability in water clarity for South Florida's marine ecosystems was examined through satellite-derived light attenuation ( $K_d$ ) coefficients, in the context of wind- and weather patterns. Reduced water clarity along Florida's coasts is often the result of abrupt wind-resuspension events and other exogenous factors linked to frontal passage, storms, and precipitation.  $K_d$  data between 1998 and 2013 were synthesized to form a normalized  $K_d$  index (KDI) and subsequently compared with Self Organizing Map (SOM)-based wind field categorizations to reveal spatiotemporal patterns and their inter-relationships.  $K_d$  climatological maximums occur from October through December along southern sections of the West Florida Shelf (WFS) and from January through March along the Florida Straits. Spatial clusters of elevated  $K_d$  occur along 3 spatial domains: central WFS, southern WFS, and Florida Straits near the Florida Reef Tract, where intra-seasonal variability is the highest, and clarity patterns are associated with transitional wind patterns sequenced with cyclonic circulation. Temporal wind transitions from southerly to northerly, typically accompanying frontal passages, most often result in elevated  $K_d$  response. Results demonstrate the potential of using synoptic climatological analysis and satellite indices for tracking variability in water clarity and other indicators related to biological health.

**Keywords:** water clarity, satellite  $K_d$ , winds, synoptic climatology, Self-Organizing Map, Florida

\*Correspondence to: Douglas E. Pirhalla, National Oceanic and Atmospheric Administration, National Ocean Service, 1305 East West Hwy, Silver Spring, MD 20910, USA; E-mail: [doug.pirhalla@noaa.gov](mailto:doug.pirhalla@noaa.gov)

**Received:** September 1, 2016; **Accepted:** September 30, 2016; **Published Online:** October 30, 2016

**Citation:** Pirhalla D E, Sheridan S C, Lee C C, *et al.* (2016). Water clarity patterns in South Florida coastal waters and their linkages to synoptic-scale wind forcing, *Satellite Oceanography and Meteorology*, vol.1(2): xx-xx. <http://dx.doi.org/10.18063/SOM.2016.02.003>

## 1. Introduction

South Florida encompasses a unique coastal environment as epitomized by its clear subtropical waters, vast biodiversity of living marine resources, and touristic appeal. In particular, the oligotrophic waters surrounding the Florida Keys, Florida Reef Tract, Florida Bay, and Florida Shelf systems are

home to a wide array of distinct coral, seagrass, marine reptile, and fish species. These waters are also internationally known for their commercial and recreational value for scuba diving, fishing, and beach use. Despite the vast ecological services and critical attributes contained in these waters, the entire region is under constant threat from increased human activities and climate/weather disturbances including a pos-

itive trend in tropical cyclone activity, extreme precipitation, flooding, and storm surge (Kunkel, Karl, Brooks *et al.*, 2013; Martinez, Maleski and Miller, 2012; Obeysekera, Park, Irizarry-Ortiz *et al.*, 2011). Consequently, one of the most immediate impacts from these disturbances is on coastal water clarity, as substantial runoff, sediment, and particle resuspension can often lead to significant degradation in water clarity and quality, affecting all marine animals and plants that rely on ambient light.

Typically expressed as light attenuation (or  $K_d$ ; the vertical attenuation coefficient for downward irradiance), water column clarity is dependent upon four major water quality agents: 1) re-suspended or terrestrial input of inorganic sediments; 2) chromophoric dissolved organic matter (CDOM); 3) chlorophyll; and 4) other suspended particulate matter (Biber, Paerl and Gallegos, 2005; McPherson, Hill, Zimmerman *et al.*, 2011). In combination, these constituents influence absorption and scattering of light with depth and the overall light regime available for plants and animals. In both optically deep and shallow waters, satellites have proven useful for capturing changes in water clarity over fairly short time scales (Barnes, Hu, Schaeffer *et al.*, 2013; Barnes and Hu, 2015; Hu, Barnes, Murch *et al.*, 2014; Palandro, Hu, Andréfouët *et al.*, 2004). Barnes *et al.* (2013) used high resolution  $K_d$  imagery and optimized algorithms from NASA's Moderate Resolution Imaging Spectroradiometer (MODIS) on the satellite Aqua to characterize spatiotemporal water clarity patterns and variability in the optically shallow waters of the Florida Keys. While Barnes *et al.* (2013) generally found low variability in water clarity for the Florida Reef Tract, strong variations in clarity can occur elsewhere throughout the region and throughout the year. In terms of the accuracy of satellite-based  $K_d$  data, Barnes and Hu (2015) made a comparison of  $K_d$  estimates across three sensors: Sea-viewing Wide Field-of-view Sensor (SeaWiFS); MODIS, and Visible Infrared Imager Radiometer Suite (VIIRS) sensors; and found strong agreement in retrievals for most of the South Florida region. The overall assessment of water clarity changes in response to climate variability, compounded by human activities, requires consistent observations from multiple sensors, over frequent temporal scales, and with synoptic coverage (Hedley, Roelfsema, Chollett *et al.*, 2016).

Multiple factors contribute to changes in optical properties that influence water clarity conditions in

South Florida coastal waters. Excessive rainfall/discharge events in combination with seasonal and abrupt storm and cold front passage can force sediment and particle resuspension, alter CDOM and nutrient delivery into the coastal zone and trigger changes in the water column constituents that impact clarity (Hu, Muller-Karger and Swarzenski *et al.*, 2006; Hu, Hackett, Callahan *et al.*, 2003; Hu, Muller-Karger, Vargo *et al.*, 2004; Le, Hu, English *et al.*, 2013; Lohrenz, Wiesenburg, Arnone *et al.*, 1999; Ransibrahmanakul and Stumpf, 2002; Barnes, Hu, Schaeffer *et al.*, 2013; Lee, Johns, Wilson *et al.*, 2002). Excessive and widespread phytoplankton blooms and "black water" events contribute substantially to changes in water column constituents (Hu, Hackett, Callahan *et al.*, 2003; Hu, Muller-Karger, Vargo *et al.*, 2004; Hu, Muller-Karger and Swarzenski, 2006; Conmy, Coble, Cannizzaro *et al.*, 2009; Neely Bartels, Cannizzaro *et al.* 2004). Conmy *et al.* (2009) attributed major changes in the underwater light field of the West Florida Shelf (WFS) to tropical and extratropical storms, discharge, and resuspension events, hinting at the profound influence of wind forcing on water constituents in the region. The overall influence of synoptic systems such as storms and cold fronts in combination with discharge, winds and transport likely co-contribute to water clarity changes at sub-regional scales, especially in Florida Shelf and Florida Keys systems where upwelling/mixing and transport of materials "downstream" of river sources can occur (Del Castillo, Gilbes, Coble *et al.*, 2000; Hu, Muller-Karger, Vargo *et al.*, 2004; Lee, Johns, Wilson *et al.*, 2002; Gramer, 2013).

Linking the influence of weather systems such as storms, cold fronts, and other patterns with in-water impacts provides a useful tool for understanding causal mechanisms and improving predictions of critical light field changes. To better understand the role of weather patterns and climate variability on water quality variable response in South Florida, Sheridan *et al.* (2013) applied progressive synoptic-to-satellite techniques to isolate weather patterns linked to elevated chlorophyll levels and algal blooms. Pirhalla *et al.* (2014) followed using similar techniques to isolate lethal cold-season atmospheric patterns and ocean-sea surface temperature (SST) anomalies linked to biological stress and mortality in marine life. Lee *et al.* (in review) further used synoptic methods coupled with a non-linear neural network-based time series

model to develop long term historical reconstructions of water clarity for southeast coastal waters. Although these studies largely attribute in-water impacts to specific *weather situations* over longer temporal scales (e.g., monthly to interannual time scales), more abrupt perturbations, particularly with circulation-induced resuspension and water events, were not addressed. Consequently, unanswered questions remain about the connections between water events and wind patterns, especially in areas where cumulative wind-wave stress, turbidity, and sedimentation may be a limiting factor to biological health and mortality (e. g., coral and seagrass loss or die-offs). Through this work, we attempt to better define the role of winds on clarity patterns, and further resolve the spatial and temporal scales related to wind influences on historical water quality-related events that have impacted the region over nearly the last two decades.

In this paper, we extend our previous work in applying synoptic climatological analysis to marine ecosystem response, and examine synoptic-scale wind fields in relation to water clarity and turbidity events. We use synoptic methods to identify and define the wind patterns and temporal transitions most connected to the variability exhibited in  $K_d$  for South Florida, with emphasis on elevated turbidity events in surrounding areas of the West Florida Shelf, Florida Keys, Florida Straits, and within the Florida Keys National Marine Sanctuary. This investigation was conducted through a blending of  $K_d$  light index products and self-organizing maps of wind fields to characterize the spatiotemporal extent of poor (and optimal) water clarity patterns and their association with discrete wind pattern classifications. The specific objectives were to 1) identify and define seasonal water clarity conditions and ranges (i.e., poor to optimal) for a reconstructed blended satellite  $K_d$  climatology; 2) map spatial clusters of reduced water clarity conditions due to the effects of wind forcing through image compositing of  $K_d$  and wind SOMs; and 3) evaluate synoptic transitions of wind patterns and coincidence with satellite-derived light attenuation index along areas of the West Florida Shelf, Florida Reef Tract and Florida Straits.

## 2. Materials and Methods

### 2.1 Atmospheric Data Processing and Synoptic Classification Using Self-Organizing Maps

For atmospheric processing and wind analysis, daily wind fields of mean meridional ( $v$ ) and zonal ( $u$ ) 10-meter component data were obtained from the North American Regional Reanalysis (NARR; Mesinger *et al.*, 1996) project website (Table 1). Specifically, data for the 727 gridpoint locations encompassed by the spatial domain spanning 30°N to 24°N and 78°W to 88°W, and the temporal domain spanning 1 January 1979 to 30 June 2014 were acquired. The 1454 wind components (2 components each at 727 locations) were first standardized and then subjected to an s-mode principal components analysis (PCA), with the resulting principal component scores (PCs) retained as the input data into the classification. Developed by Kohonen *et al.* (1995), self-organizing maps (SOMs) are a clustering methodology increasingly employed by synoptic climatologists over the past two decades (e.g., Cavazos, 1999; Hewitson and Crane, 2002; Sheridan and Lee, 2011). Unlike traditional clustering methods, SOMs are able to order the resultant clusters (e.g., synoptic-scale wind patterns) onto a multi-dimensional plane, with similar clusters adjacently located in this ‘SOM-space,’ and dissimilar patterns spaced further apart (Hewitson and Crane, 2002). This structure to the classification allows for a more intuitive visualization of circulation-based synoptic patterns and their impacts on any climate-related outcome (e.g., water clarity; Sheridan and Lee, 2011). For a detailed discussion on the use of the SOM methodology in synoptic climatology, please see Hewitson and Crane (2002) and Sheridan and Lee (2011).

All SOM procedures were completed using MatLab version 2013b with the Neural Network and Statistical Toolboxes. Since the first two PCs accounted for nearly equal variance (41.8% and 38.5%, respectively) in the standardized wind data set, and the preliminary shape of the SOM is based upon the space encompassed by the two leading principal components of the input data, a nearly square 6x5 SOM was selected.

**Table 1.** Data products analyzed in this research

Sensor/ Platform	Time span	Variables	Coverage	Frequency	Quality	Source
NA Regional Reanalysis	1979–2014	U- and V-Winds	32km grid	Daily	High	NCEP, ESRL/PSD
SeaWiFS	1997–2010	$K_d$ 490	1 km grid	Near daily	High	NASA
MODIS	2002–2014	$K_d$ 488	1 km grid	Near daily	High	NASA

The MatLab default learning rates were used for the ordering (0.90) and tuning (0.02) phases of the SOM algorithm, the initial neighborhood distance was set equal to the maximum distance between SOM-nodes (5), and the SOM algorithm was set to iterate 10,000 times. MatLab's default hexagonal topology was changed to the more traditional grid-shaped topology in order to conform to most SOM-based synoptic climatological research (e.g., Cassano, Gilsan, Cassano *et al.*, 2015; Hewitson and Crane 2002); and the distance linking function was changed to 'boxdist' in order to properly accommodate this topology (MatLab, 2015). After running to completion, the SOM essentially classifies each day into one of 30 wind patterns (WPs) based upon the similarity of that day's synoptic-scale wind pattern with those of all other days in the data set. Component (vector) averaged wind speed and wind directions within the domain were computed separately for each of the 30 resultant WPs and mapped using the MatLab Mapping Toolbox. This gridded topology of the SOM results in a 2-dimensional lattice of wind patterns.

## 2.2 Satellite Data Processing and $K_d$ Climatology

Satellite data used in the study consist of blended  $K_d$  imagery and time series from two different NASA sensors: (1) SeaWiFS and 2) MODIS onboard the satellite Aqua (MODIS/A; Table 1). Reflectance data from both sensors were used to derive  $K_d$  data products including the standard  $kd\_lee$  (Lee, Darecki, Carder *et al.*, 2005; Lee, Lubac, Werdell *et al.*, 2009) and a modification of the  $K_d\_lee$  algorithm validated for optically shallow water applications (Barnes, Hu, Schaeffer *et al.*, 2013). The entire time series of SeaWiFS and MODIS Level-2 ocean color data within the bounds of 24° to 31°N, 78° to 98°W were acquired from NASA Goddard Space Flight Center. From these, the  $K_d\_lee$  algorithm and its modification were applied to the mapped  $R_{rs}$  data to derive  $K_d(488)$  for optically deep and shallow targets in South Florida. Pixels with negative  $R_{rs}$  were excluded from analysis as were pixels identified as low quality by the Level-2 processing flags (see Barnes and Hu, 2015; for specific flags used). Prior to analysis, all  $K_d(488)$  values were log-transformed to make their distributions normal. Next, using both SeaWiFS and MODIS data, daily mean images were created for each day from 1997–2013. A 3×3 mean spatial and 3 day mean temporal filter was applied to all  $K_d(488)$  scenes, whereby pixels were excluded if any previously masked pixels

(either due to negative  $R_{rs}$  or Level-2 processing flags) were within the 3×3 window with the pixel of interest in the center.

Barnes *et al.* (2013) applied empirical orthogonal function analysis to separate dominant modes of  $K_d$  variability in Florida Keys waters and concluded the seasonal cycle explained over 85% of the variation in  $K_d$ . To estimate seasonal and higher frequency patterns of  $K_d$  variability for the entire domain, we constructed a daily-scale  $K_d$  climatology as:

$$\overline{Kd}_J = \frac{\sum_{t=0}^n Kd_t}{n} \quad (i)$$

Where  $\overline{Kd}_J$  is the climatological mean  $K_d$  on Julian day  $J$ ,  $Kd_t$  is the 3-day mean log-transformed  $K_d$  at time  $t$ , and  $n$  is the number of valid satellite observations at that pixel during the time frame  $t$ . We used the climatology to compare selected upper and lower quantiles and first order statistics to highlight spatial  $K_d$  patterns and general timing of  $K_d$  events and water clarity patterns. Individual  $K_d$  pixel values were first rank ordered over their entire distribution then grouped by quantile level as: <5<sup>th</sup> (extremely clear), 5<sup>th</sup>-25<sup>th</sup> (clear), 75<sup>th</sup>-95<sup>th</sup> (poor and), and >95<sup>th</sup> (extremely poor). Pixels for which the value of the 5th percentile was greater than 0.1 m<sup>-1</sup> were removed prior to further analysis due to likely bottom contamination. Pixels showing elevated values in the 5<sup>th</sup> percentile level greater than 0.1 m<sup>-1</sup>, were likely due to bottom contamination and removed prior to further analysis.

Finally,  $K_d$  products from MODIS and SeaWiFS were blended to create a moving index of  $K_d$  departure from climatological normal, termed  $K_d$  index or KDI. KDI was calculated using the filtered  $K_d$  time series with moving pixel values standardized to account for seasonal effects and areas of differing water clarity (e.g., chronically turbid areas) using:

$$KDI_t = \left( \frac{(Kd_t) - (\overline{Kd}_J)}{\sigma_J} \right) \quad (ii)$$

Where KDI at time  $t$  is the difference between the 3-day moving  $K_d$  at time  $t$  and the climatological mean  $\overline{Kd}$  observed on Julian day  $J$ . The difference is normalized by its standard deviation term,  $\sigma_J$

$$\sigma_J = \sqrt{\frac{\sum_{i=0}^n ((Kd_t) - \overline{Kd}_J)^2}{n-1}} \quad (iii)$$

The KDI, normalized by the mean and divided by standard deviation, enables comparison of pixels from different locations with different mean conditions, and highlights areas with greatest temporal deviation. As a result,  $K_d$  and KDI imagery reveal unique spatial patterns during specific events over the South Florida region. All atmospheric,  $K_d$  and KDI data analyses were performed for all calendar months. Image pixels were extracted and analyzed along a transect spanning 3 biogeographic sub-regions: central West Florida Shelf (WFS), Florida Keys (gulf side), and Florida Straits near the Florida Reef Tract, through pixel-based extractions along the transect line.

The study area and spatial domain for wind extractions and satellite image analysis is shown in Figure 1A. During specific  $K_d$  events, spatial patterns of increased light attenuation can be detected from MODIS imagery (Figures 1B and C). This single day image acquired February 10, 2010 shows a high- $K_d$  event that significantly reduced the underwater light field along sections of the West Florida Shelf, including parts of the Florida Reef Tract (Barnes *et al.*, 2013). Elevated  $K_d$  and KDI values ( $>3$ ) were evident for an extended period from mid-January through March,

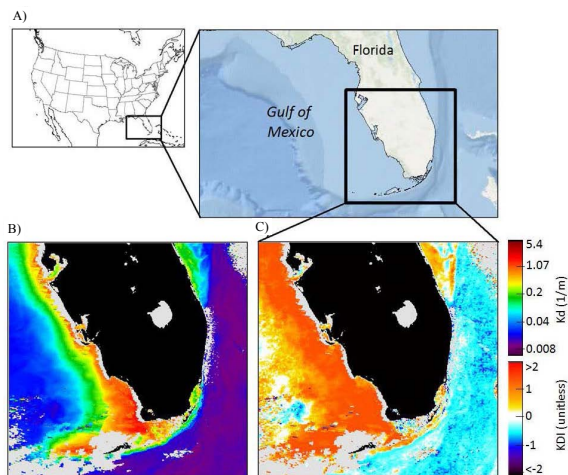


**Figure 1.** Study area and domain for NARR wind extractions and NASA  $K_d$  image analysis (A). MODIS 1 km  $K_d$  imagery for February 10, 2010 (B), represent water clarity conditions and its corresponding KDI (C) showing increased  $K_d$  (i.e., reduced clarity) for the eastern portion of the region of interest. KDI was derived as log-transformed  $K_d$  for February 10, 2010, minus the climatological mean  $K_d$  for February 10 of 1997–2013, normalized by  $K_d$  standard deviation. Default  $K_d$  products (used in optically deep waters) are available from NASA Ocean Biology Processing Group, while KDI products modified for optically shallow waters are available from University of South Florida (USF) and NOAA. Ocean/World base map layer was provided by Esri, DeLorme, GEBCO, NOAA NGDC, and other contributors.

2010. The event occurred during a time of active and severe weather including a cold-air outbreak and cold-snap event of extreme duration, causing region-wide air and sea surface temperatures to drop well below tolerance levels for multiple animal species (Pirhalla, Sheridan, Ransibrahmanakul *et al.*, 2014; Roberts, Collins, Paxton *et al.*, 2014; Lirman, Schopmeyer, Manzello *et al.*, 2011).

### 2.3 Estimating Water Clarity Patterns from Wind SOM Node Occurrences

To gain a better understanding of classified wind pattern effects on water clarity conditions, normalization procedures taken from Sheridan *et al.* (2013) were used to develop climatological KDI monthly image composites, computed as the ratio of median KDI conditions for the SOM node (WP) of interest to the expected median KDI condition for all nodes (WPs). That is, for each WP in each calendar month, the ratio of KDI median only for dates when the node of interest occurred over the grand median was calculated as:

$$\text{KDI Deviation}_{J,WP} = \frac{(\text{Md KDI}_{J,WP_x})}{(\text{grand Md KDI}_{J,WP_{S_{1-30}}})} - 1 \quad (\text{iv})$$

where  $\text{Md KDI}_{J,WP_x}$  is the median KDI associated with  $WP_x$ , and similarly,  $\text{grand Md KDI}_{J,WP_{S_{1-30}}}$  is the climatological median KDI for all WPs. Spatial clusters of elevated water clarity patterns for each node were mapped in SOM-space by month, then averaged for the months of November through March.

To further evaluate individual WP spatial association with elevated KDI, a second metric, SOM WP node percent deviation during elevated KDI conditions, was computed. For each climatological month of the year, we calculated this metric as the probability of a WP occurring when  $\text{KDI} > 1.5$ , subtracted by the random probability of all 30 WPs under all KDI conditions. This calculation was performed to standardize WP percent deviation across all 30 WPs. The percent deviation metric represents the likelihood of  $WP_x$  occurring when  $\text{KDI} > 1.5$  compared to what would be expected for all 30 WPs purely by random chance. For example, if  $WP_x$  occurred 25% of the time when  $\text{KDI} > 1.5$ , and all 30 WPs had a random probability of 3.33% for all KDI conditions, the WP node percent deviation would be +21.67%.

In addition to identifying individual wind patterns associated with elevated  $K_d$  patterns during the day of

a  $K_d$  event, we also tested whether *transitions* from one WP to another were associated with a  $K_d$  event. This involved using a 3-day window prior to  $K_d$  events ( $KDI > 1.5$ ) to bin the most frequent nodes that resulted in elevated  $K_d$  values across the domain. For

$$\sum \begin{cases} WP_x \text{ occurring 1 to 3 days prior to } K_d \text{ event} & \rightarrow \text{counts(days)} \\ WP_y \text{ occurring at time } t \text{ of } K_d \text{ event} & \rightarrow \text{counts(days)} \\ WP_{x,y} \text{ node combinations} & \rightarrow \text{counts(days)} \end{cases}$$

WPs that most often occurred 1–3 days prior to a WP with a high ( $> 1.5$ ) median  $KDI$  value were identified to reveal the importance of specific wind transitions linked to elevated  $K_d$  conditions.

### 3. RESULTS

#### 3.1 Water Clarity Patterns of Variability

The climatological cycle of  $K_d$ 488 across the artificial transect line is depicted in Figure 2. The annual  $K_d$  cycle from January through December (Figures 2B–C) reveals  $K_d$  mean and standard deviation, respectively. Mean  $K_d$  ranges from approximately  $0.01 \text{ m}^{-1}$  in open waters of the West Florida Shelf, to near  $1 \text{ m}^{-1}$  seaward of Charlotte Harbor, FL. During the au-

example, if  $WP_x$  occurred 1 to 3 days prior to a  $KDI$  event,  $WP_x$  was binned with the event *and* the associated  $WP_y$  at the time of the event. Counts of the leading WPs prior to  $KDI$  event were summed then rank ordered across SOM- space as:

tumn-winter cycle, a sharp  $K_d$  spatial gradient appears separating nearshore higher attenuation (more turbid) areas near Sarasota, Charlotte Harbor, and Key West, FL from lower attenuation (less turbid) areas along the WFS and Florida Strait. During winter, Figure 2B shows  $K_d$  values ranging from  $0.5 \text{ m}^{-1}$  along the 10 m isobath seaward of Sarasota, FL to Charlotte Harbor, FL (A–B),  $0.5 \text{ m}^{-1}$  north of Key West (C), and near  $0.04 \text{ m}^{-1}$  south of the Florida Keys in the Florida Strait (E–G). Temporal patterns of  $K_d$  in Figure 2C reveal greater variability during autumn, winter and early spring in northern and southern sections of the transect (A–B; C–D; E–G), with an abrupt decrease in variability evident in mid-April.

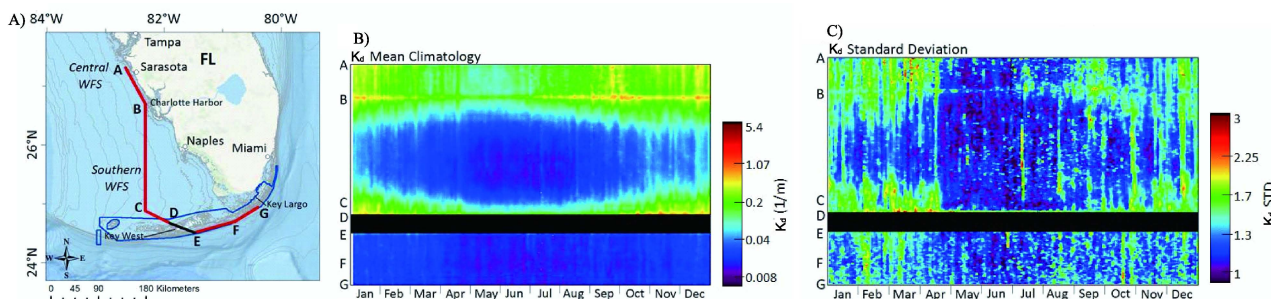


**Figure 2.** Map of study region (A) and Hovmöller diagrams of b)  $K_d$  mean and c) standard deviation over a climatological annual cycle, derived for 1997 to 2013. Hovmöller plots show daily running mean  $K_d$  distribution (B, top) and variability (C, bottom) over an annual cycle along a north-south latitudinal transect line (A–D) from approximately Sarasota, FL to Key West, joined with a longitudinal line along the 30 m isobath from Big Pine Key to approximately Key Largo (E–G).

More detailed within-season spatial variations in water clarity are shown in Figure 3, which separates the  $K_d$  climatology into quantiles of extremely clear water to extreme turbid water. Each pixel was sorted by most prominent month of occurrence within each quantile bin. Spatial variations in months of turbid conditions (Figure 3C) show an autumn to winter preference in elevated  $K_d$  signals, especially in November–December along the WFS, January for offshore areas, and February–March along the Florida Straits near the Florida Reef Tract. Lower quantile

ranges show most prevalent clear water months (a–b) to be March–April in nearshore areas and in April–May along the WFS. In offshore areas especially along the Florida Current, water clarity is generally clearest in July–August.

#### 3.2 SOM-based Wind Patterns (WPs)

Using the SOM-based clustering procedures outlined above, the resulting classification of wind patterns across the domain and each pattern’s monthly frequency are displayed in Figure 4. The wind patterns

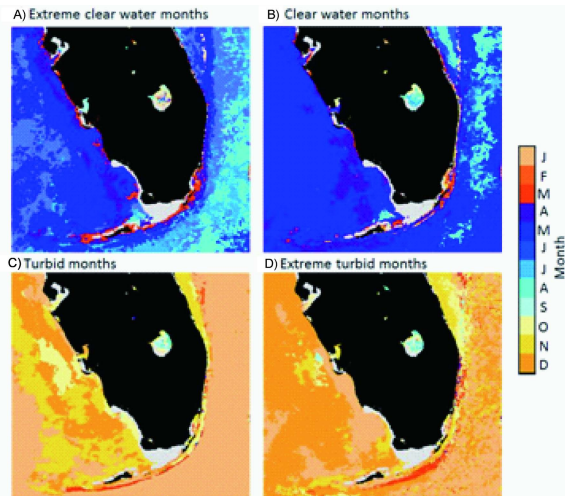


**Figure 3.** Timing of clear and turbid water within a typical season. All available  $K_d$  images were binned within quantile ranges: A) 0%–5%, B) 5%–25%, C) 75%–95%, and D) 95%–100%, and the most prominent month of occurrence was calculated for each pixel. Extremely clear (A; top) and clear water months (B; top) indicate when clearest waters are found in a typical season. Turbid (C; bottom), and extreme turbid water months (D; bottom) indicate when turbid waters are found in a typical season.

are broadly arranged in ‘SOM-space’ with the stronger magnitude winds around the outside columns and rows, and weaker wind patterns towards the middle of SOM-space. In terms of wind direction, generally winds shift from westerly to easterly from left to right across SOM-space, and from southerly to northerly from top to bottom – exhibiting the organizing nature of the SOM procedure. The Sammon Map (Figure 5) shows the relative (dis)similarity between neighboring and distant patterns in terms of distance in SOM-space. For example, the differences between WPs along the top row of the SOM are not as great as the differences between WPs 1–6 along the bottom row – as evidenced by the longer distance between patterns 1–6 compared to the distance between patterns 25–30.

The resultant wind patterns displayed herein compare favorably with previous research on seasonal wind and circulation features evaluated for south Florida (Liu and Weisberg 2012; Mitchum and Sturges, 1982) with generally stronger north and west wind patterns in winter and lighter southerly winds in summer, moving anti-cyclonically around the Bermuda High.

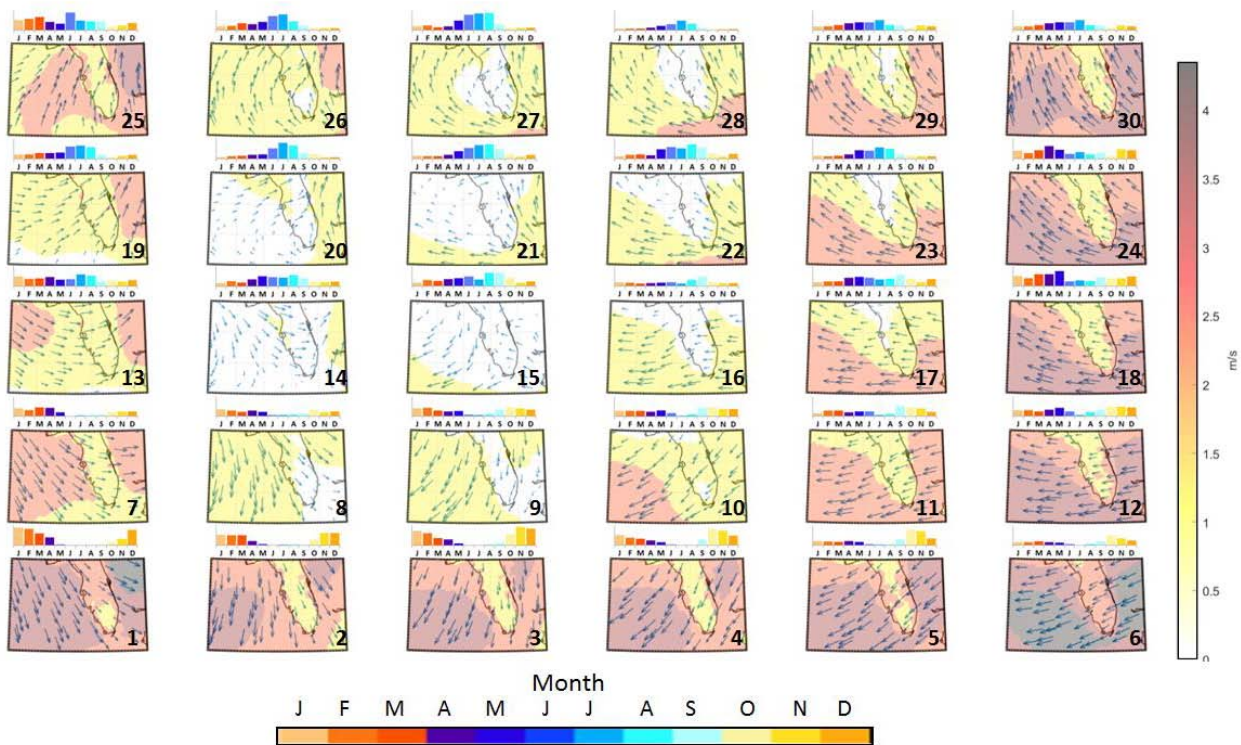


**Figure 4.** SOM-based network of wind pattern nodes of mean daily near-surface (10 m) wind speed (colors) and direction (arrows) when each wind pattern (WP) occurs. WP numbers are indicated in the lower right hand corner of each node. Average monthly frequency (from January to December) of each WP is indicated by the bars above each map, with the top of bar-graph’s vertical axis indicating 10% frequency in each month. WP node 1 (bottom left corner) represents a winter dominant pattern with generally strong northwesterly daily wind fields.

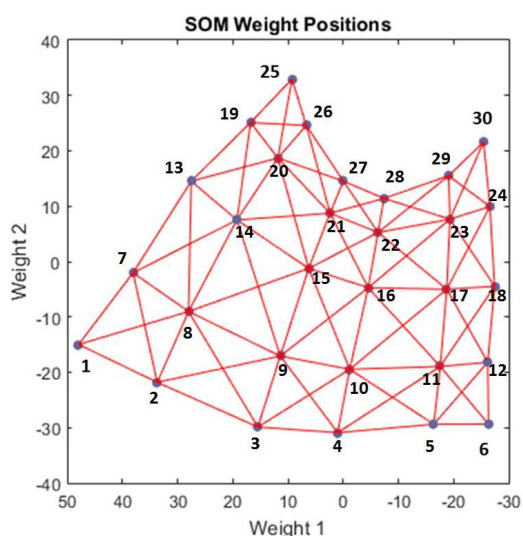


**Figure 5.** Sammon map for Wind SOM shown in Figure 4

Along the bottom row in Figure 4, moving right to left (i.e., from WP6 to WP1) there is a marked transition from autumn-dominant patterns to winter-dominant patterns, with strong north-easterly winds stemming from a continental high pressure (WP4–WP6) transitioning to north and northwesterly (WP1–WP3) as mid-latitude synoptic-scale systems begin penetrating further south, making frontal situations and regional cyclonic flow more frequent. Over the course of autumn as the summer trade winds wane and mid-latitude weather becomes more influential, a stronger northerly component to the wind becomes noticeable (Liu and Weisberg 2012). Eventually light and variable trade winds and anticyclonic flow again dominate in the summer, as shown with the WPs in the top middle of the SOM (i.e., WPs 15–17; 20–23; 26–29).

In addition to these primary seasonal modes captured by the SOM, many WPs also display secondary synoptic features within season. For example, WPs in the lower left corner of the SOM (WPs 7, 1, 2, and 3) represent common post-frontal situations with a strong northerly component to the winds. These WPs often follow the pre-frontal WPs in the upper right corner of the SOM (WPs 29, 30, 24, 18) during the transition seasons (spring & autumn), possibly catching the backside of a continental high moving offshore, but also by frontal conditions depicted by WPs on the left side of the SOM (WPs 13, 19, and 25) in all seasons.

### 3.3 Wind Patterns and $K_d$ Spatial Patterns

Results suggest a general relationship between active northerly wind patterns, frontal situations and storms, and more active periods of elevated  $K_d$  and  $K_d$  events.

In order to further isolate specific wind patterns in connection with  $K_d$  events, spatial  $K_d$  patterns and daily co-occurrence with WPs in SOM-space were evaluated in greater detail. KDI monthly median ratio (Figure 6A) and KDI percent change (Figure 6B) maps for each WP reveal elevated, neutral, or diminished KDI spatial distribution patterns during days when each WP occurred. For space considerations, months of November through March were averaged and shown in two calendars. For all 30 WPs evaluated, WPs 1, 2, and 3 (Post-frontal) along the bottom axis showed the strongest spatial association with elevated KDI in the months depicted, with a weaker association in summer (not shown). In particular, elevated KDI above median conditions were most apparent for WPs 1-3 for expansive areas along the West Florida Shelf (circles; Figure 6); WPs 4, 5, and 6 for Gulf Coast areas north of the Florida Keys; and WPs 18, 24, and 30, mainly along the Florida Strait, slightly seaward of the Florida Reef Tract. Positive KDI signals were also evident for WPs 7, 13, and 25 in winters, but less consistent across all months.

Positive KDI spatial patterns favor an association with strong northerly post-frontal patterns in SOM-space, hinting at a strong within-season influence. The strongest response was associated with WP1 with normalized KDI well above 3, indicating a greater association when winds have their greatest magnitudes and blow parallel to the western Florida coastline.

### 3.4 Wind Pattern Transitions During $K_d$ Events

While elevated anomalous  $K_d$  and KDI was most evident for WPs 1–6, a more detailed analysis of the transitional nature of the winds on days leading up to the event provides a better understanding of precursory patterns and lag-response mechanisms linked to severe turbidity events. In particular, we were interested in which WPs occurred more frequently in sequence with WPs1–3 prior to  $K_d$  event. After ranking all counts of WPs and co-occurrences with WP1, 2, or 3, from most to least frequent during elevated KDI ( $KDI > 1.5$ ), the leading nodes 1 to 3 days prior to  $K_d$  event are shown in Table 2. WPs showing highest counts (ranks) prior to  $K_d$  event were WP1 (74), WP30 (34), WP13 (29), and WP25 (28) transitioning to WPs1–3 (Table 2A). A second ranking was performed on  $K_d$  events when WPs4-6 occurred (Table 2B), showing highest counts prior to  $K_d$  event as WP1 (11), WP18 (10), WP6 (7), and WP2 (6).

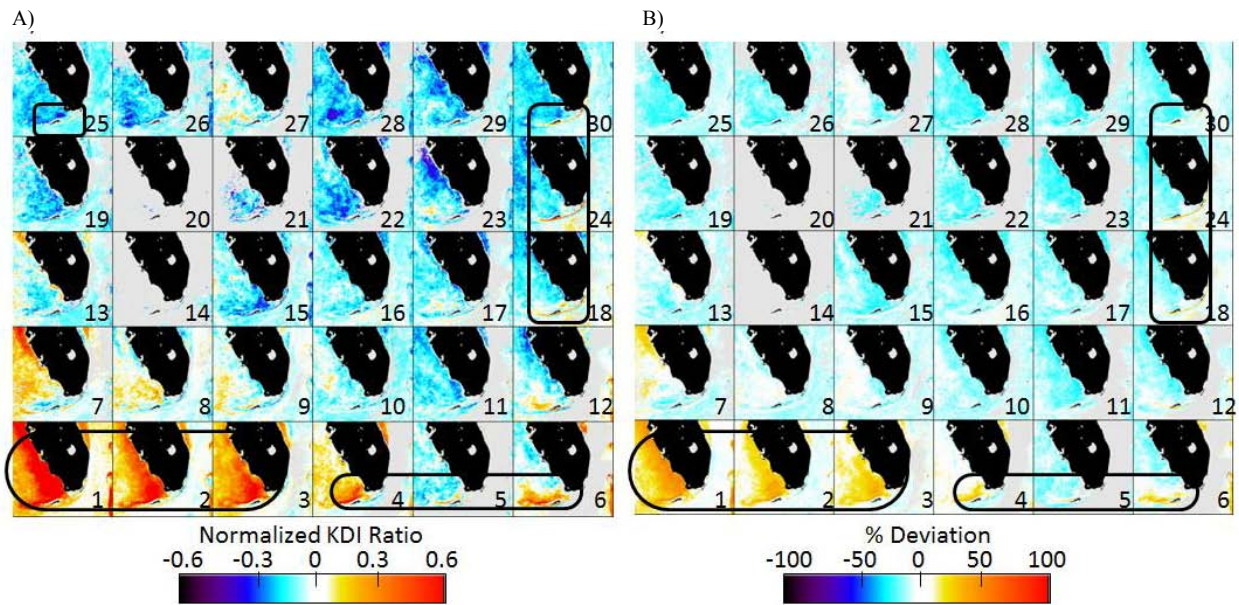


**Figure 6.** SOM-space map of blended MODIS and SeaWiFS climatological KDI associations for November–March, calculated as A) the ratio of the KDI median on dates when each WP occurred to the grand median monthly KDI value for the 16-yr period; and B) the difference between the probability of elevated KDI events for each WP and the overall probability of elevated KDI for all WPs. KDI events defined as  $KDI > 1.5$  (See methods for full description). The figure enables visualization of positive (poor clarity; orange–red in circles) and negative (good clarity; blue) KDI conditions associated with each WP. Gray areas indicate no data are available (generally because of cloud cover).

**Table 2.** Total counts (days) in SOM-space of WP nodes most often occurring 1–3 days prior to a) WPs 1, 2, or 3 along northern section of the artificial transect line (A–B; Figure 2), and b) WPs 4, 5, or 6 along southern section of transect (C–D; Figure 2) during elevated KDI ( $> 1.5$ ) conditions. Orange highlights indicate top 6 ranks. The figure enables visualization of WPs most often occurring in sequence during  $K_d$  events.

A) Prior to WPs 1, 2, or 3					
28	5	5	2	11	34
20	6	3	3	1	13
29	8	6	12	6	7
19	13	7	7	5	4
74	23	17	11	1	1

B) Prior to WPs 4, 5, or 6					
4	0	1	0	0	4
2	0	0	3	2	2
4	2	0	0	1	10
3	1	1	2	4	5
11	6	0	4	5	7

Using the rank scores of all wind sequences leading to elevated  $K_d$  conditions, the most recurring wind transitions are shown in schematic form (Figure 7) where three different transitions are identified: 1) Figure 7A reveals pre-frontal patterns (WPs 13, 19, and 25) transitioning into a post-frontal pattern, whereby gulf-origin winds shift from southwesterly, or westerly to northerly; 2) Figure 7B reveals a southeasterly pattern (30) transitioning into a post-frontal pattern, whereby winds from the Caribbean Sea shift to take on a more northerly component; and 3) Figure 7C reveals strong post-frontal patterns transitioning to a strong easterly patterns. These transitions occur predominantly between November–March and represent scenarios in which suspended particulate or

dissolved material are more likely to be re-suspended and mixed with surface waters, and subsequently transported offshore.

Composite maps of median KDI distribution for specific WP transitions are shown for November–March (Figure 8). This figure shows the spatial distribution of KDI when WP1, 2, or 3 occurred 1–3 days following incidences of WP13 (A), WP25 (B), WP30 (C), and anticyclonic WPs (14, 15, 16, 17, 20, 21, 22, 23, 27, or 28), indicating that  $K_d$  is well above normal over a large portion of the study domain when post-frontal WPs (1, 2, 3) are either preceded by pre-frontal or frontal (Figure 8A, B; WP 13, 25, or 30), but deviations are neutral or below normal when post-frontal patterns are preceded by anticyclonic patterns (Figure 8D).

Comparisons of time series of autumn/winter KDI values along the transect with daily co-occurrences of transitional WPs 1, 2, 3, 13, 25, and 30 reveal  $K_d$  events and coincidence with WP in greater detail (Figure 9).  $K_d$  peaks can be seen as both heightened

periods spanning 1–3 months (circles) and shortened pulses spanning days to weeks (arrows). For example, elevated KDI during winter and spring of 1997/1998, autumn of 2004, autumn–winter of 2005/2006 and winter of 2010 were particularly evident. Of note are

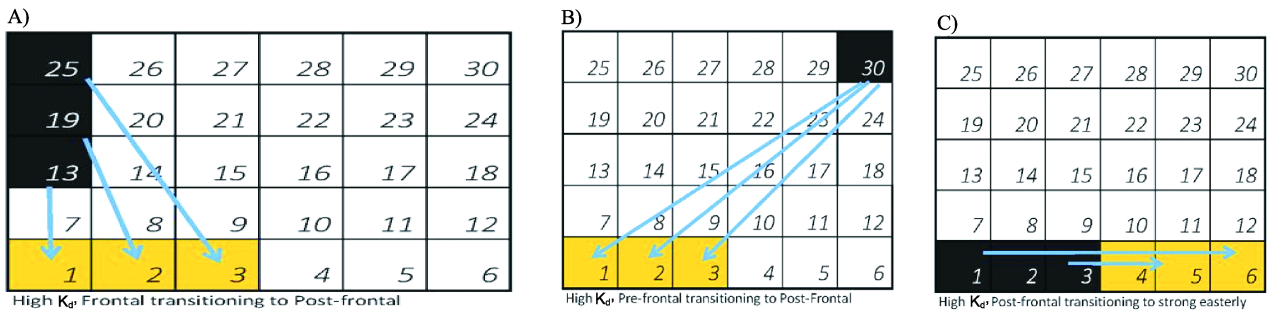


**Figure 7.** Schematic of WP transitions most associated with elevated  $K_d$  events ( $KDI > 1.5$ ). Arrows represent wind transitions 1 to 3 days prior to  $K_d$  event to day of event; A) Pre-frontal pattern 25, 19, or 13 transitioning to post-frontal patterns 1,2, or 3; B) Pre-frontal pattern 30 transitioning to post-frontal patterns 1, 2, or 3; and C) Post-frontal patterns 1, 2, or 3 transitioning to strong easterly patterns 4, 5, or 6.

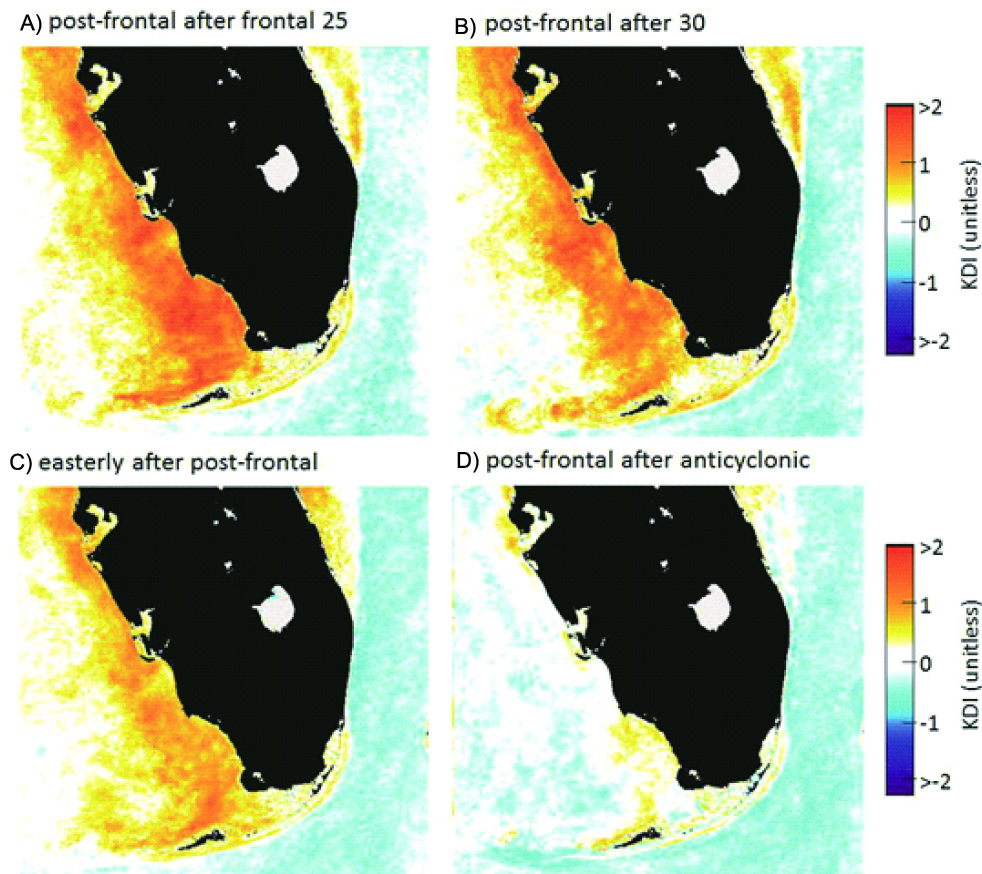


**Figure 8.** Median KDI during specified wind transitions; A) WP 1, 2, 3 (Post-frontal) following prefrontal/cyclonic WP13; B) Post-frontal following frontal WP25; C) Post-frontal following prefrontal WP30; and D) Post-frontal following anticyclonic patterns (WPs 14, 15, 16, 17, 20, 21, 22, 23, 27, or 28). KDI median was calculated for all incidences where WPs 1, 2, or 3 occurred 1 to 3 days following prefrontal, frontal or anticyclonic patterns described above. The figure enables visualization of positive (poor water clarity; orange) and negative (clear water; cyan) KDI response associated with synoptic wind pattern transitions.

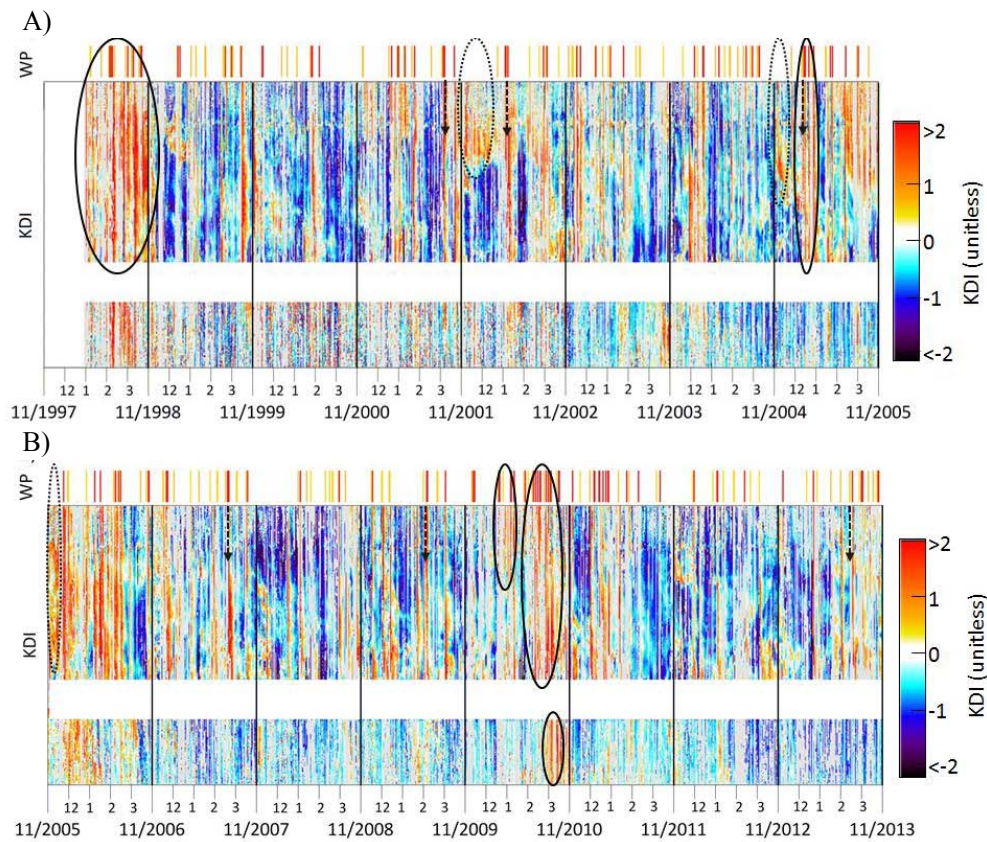


**Figure 9.** Hovmöller diagram of daily-scale KDI values along the transect from Figure 1A(A–G), calculated for 1998–2005 (A; top) and 2005–2013 (B; bottom), including data from November through March. Time series of WP combinations 1, 2, or 3 (red), 13, or 25 (yellow) and 30 (orange) are shown above KDI time series. Normalized KDI values with WPs provide visualization of  $K_d$  events and influencing mechanisms associated with short duration transitional wind fields (arrows), episodic tropical cyclones or blackwater events (dashed circles), and winter storms (circles).

the latent peaks and residuals associated with late summer–fall cyclones (dashed circles) not coinciding with transitional winds, including tropical storm Gabrielle (2001), Hurricane Charley and Tropical Depression Ivan (2004), and Hurricanes Katrina and Rita, and Tropical Storm Wilma (2005). Also apparent is the sustained KDI peak during the El Niño – Southern Oscillation winter of 1997/1998 and active increase in transitional wind patterns. Lastly are the winter storm events during December of 2004, and the aforementioned prolonged event during winter 2010 resulting in elevated KDI along the northern side of the transect beginning in January, impacting areas along the gulf side of the Florida Keys in February, moving downstream affecting the Florida Reef Tract and Florida Straits in March.

#### 4. Discussion

Water clarity in South Florida coastal waters varies across multiple time and space scales with most ele-

vated  $K_d$  conditions and variability occurring during the late autumn and winter season. Autumn to winter  $K_d$  peaks are evident along most of the WFS, with winter to early spring peaks exhibited along sections of the Florida Straits. Climatological analysis of  $K_d$  shows highest variability associated with 1) tropical cyclones in late summer and autumn, coupled with increased frontal passage and wind-resuspension events in December through February, and 2) seasonal transitions typically in November and March, with the most elevated  $K_d$  along the Florida Straits just outside of the Florida Reef Tract occurring in March.

In terms of within-season  $K_d$  variability, during the initial weeks of the cold season in autumn, stronger northeasterly and northerly winds coincide with generally higher  $K_d$  values regionally. During the onset of the winter season after several fronts pass and particle resuspension occurs more frequently, the highest values of  $K_d$  are evident. During the spring transition in March–April and into the summer wet season, flow is

dominated by a southeasterly circulation, when the region is under Bermuda High-dominated flow with anticyclonic regional circulation (Sheridan *et al.*, 2013) at a time when generally lower  $K_d$  conditions prevail.

#### 4.1 SOM-Space patterns and implications to water clarity processes

Wind effects on  $K_d$  response vary substantially across SOM-space. WPs along the lower horizontal axis were linked to elevated, heterogeneous  $K_d$  spatial response, with more shelf-wide response in association with WPs 1–3, and southern shelf response in association with WPs 4–6. This may be due to transport, dispersal and/or settling of re-suspended materials from the north to the south after the initial  $K_d$  event, or renewed resuspension of materials north of the Florida Keys due to topography and strong easterly component winds unique to WPs 4–6. WPs (13, 19, 25, and 30) along the left and right vertical axes appear to respond in sequence with bottom horizontal axis nodes, especially during heightened  $K_d$  situations, with the key linkage being frontal and prefrontal WPs occurring 1–3 days before post-frontal WPs. The occurrence of WPs 13, 25 and 30 are most consistently observed with WPs 1–3, and likewise sequenced with elevated  $K_d$  values. WPs 13 and 25 did not show elevated  $K_d$  response when analyzed alone. Similarly, incidences of WPs 1–3 preceded by anti-cyclonic patterns did not show elevated  $K_d$  response (Figure 8).

The presence of transitional winds associated with strong southerly, followed by strong northerly wind patterns over consecutive days is quite likely the most prominent wind scenario related to elevated  $K_d$  levels. We consider WP 13 and WP 25 to be most similar to a pre-frontal or cyclonic situation whereby precipitation may ensue and add to the effect on enhanced  $K_d$  signals. Although not presented in this study, WP 25 had the highest median precipitation for any node. WP 30 was most consistent with extreme precipitation and highest mean precipitation during autumn and winter months only. WP 25 is associated with stronger southwesterly flow over the entire domain, enhanced gulf/tropical moisture, and possible instability. Consequently, WP 30 showed a similar increase in southeasterly flow over the entire domain.

#### 4.2 $K_d$ Events and Causal Factors

In assessing overall causal factors to  $K_d$  events presented as part of this paper, two modes of variability are speculated to promote anomalous increases in  $K_d$

as expressed in the KDI. The primary mode relates to episodic tropical cyclones, discharge events and expansive bloom periods that can impact the regional clarity patterns over monthly time scales. This was particularly evident for the enhanced  $K_d$  residuals in the autumn of 2001, winter of 2002, and autumn of 2004/2005. These events generally coincided with elevated precipitation associated with tropical storms, active black water events and/or water column mixing, as was the case in winter 2001/2002, where a large black water event occurred simultaneously with a diatom and toxic red tide bloom along West Florida Shelf (Hu, Hackett, Callahan *et al.*, 2003). The co-occurring blooms combined with water containing large amounts of CDOM causing increased light attenuation throughout the period. The secondary mode relates to shorter term  $K_d$  spikes associated with winter storms and extremely active weather situations with increased cold front passage and transitional wind fields. This was particularly evident during the winter storm event in December 2004 (Conmy, Coble, Cannizzaro *et al.*, 2009), and the January–March, 2010 event. Wind patterns during these events are speculated as major contributors to sediment resuspension/transport and particle release from red tide or diatom blooms in nearshore waters and  $K_d$  spikes in the time series. We suspect water clarity variability is driven by the primary in-water factors mentioned above coupled with the effects of wind resuspension, and wind-induced transport.

Although multiple limiting factors are responsible for water clarity changes in South Florida, studies involving direct wind influences on clarity are few. We believe wind mechanisms are inherent to elevated spatial  $K_d$  signals and possible impacts on habitats and species, mainly due to the profound triggering influence of winds on bottom sediment and suspended particle mixing, dispersal and transport. Black water discharge events and large algal blooms may not cause widespread clarity issues until the direct influences of the wind forcing acts as a dispersal agent transporting materials downstream from riverine sources.

During the active and extreme weather in January–March of 2010, decreased water clarity was evident throughout the region (Figure 7). Excessive KDI values were observed for the middle Florida Keys, and WFS, for two months' worth of observations, yet the area was not directly impacted by a tropical cyclone the fall of 2009, or excessive bloom activity prior to the event (Hu, unpublished data). Barnes *et al.* (2013)

summarized that north-to-south wind disturbances likely altered sub-tidal transport through channels along the Florida Keys, thus contributing to spikes in  $K_d$  during that event.

In addition, dynamical features including subtidal currents, mesoscale eddies and upwelling/downwelling episodes influence particle transport along the Florida Shelf and Florida Reef Tract and are influenced heavily by local and regional wind-forcing (Liu and Weisberg, 2012; Gramer, 2012). Heightened  $K_d$  north of the Florida Keys are likely influenced by transport processes, and vertical and horizontal mixing; whereas areas along the WFS are likely influenced more through direct discharge, related oceanographic currents, and wind-induced Ekman transport/upwelling, exacerbated by transitional wind fields. Finally, areas south of the Florida Keys along the Florida Reef Tract and Florida Straits are typically exposed to increased onshore flow especially during spring/autumn transition months, with associated upwelling, wave and tidal amplitude influence, and enhanced horizontal mixing (Gramer *et al.*, 2008; Gramer, 2013) from eddies, likely causing enhanced  $K_d$  signals just south of the Reef Tract.

## 5. Summary and Conclusion

Wind is a key variable in determining changes in sediment resuspension and water clarity patterns. Winds are dominant mechanisms for coastal transport, influencing mixed layer depth, photic depth, wave height and tidal amplitude. This investigation sought to identify key wind nodes and patterns that showed a strong association with elevated  $K_d$  and KDI values. Since  $K_d$  spatial response was strongly linked to certain wind patterns, specifically WPs 1–6, 13, 25, and 30, we believe the SOM-based methods presented here provided unprecedented resolution to the key synoptic-scale influence of winds on water clarity. The specific wind patterns borne out of synoptic climatological methods can be used to develop precursory early warning signals for water clarity events, especially considering the lagged effect of WPs on the days preceding these events.

The importance of synoptic-scale winds in the expression of water clarity patterns has many implications in coastal resource and water quality management issues in Florida. Firstly, regional wind patterns and forcing may have profound implications in terms of climate change influence. Wind response is a ma-

nifestation of the overlying circulation. Climate change will likely bring about changes to atmospheric circulation and cases of extreme weather events (Francis and Vavrus, 2012), with subsequent changes in wind forcing and storms along the Florida coast. Thus, our focus on synoptic-scale winds may be useful in helping downscale global circulation changes to local water clarity changes in response to climate change. Secondly, both acute and prolonged cases of reduced water clarity can be consistently measured through satellite imagery. We believe the blended satellite data products of KDI and wind derivatives presented herein provide more than adequate resolution of wind-resuspension processes and spatial coverage needed for predicting water clarity changes, and thus can be effective tools for South Florida's water quality management programs. In addition, satellite observations of water clarity can be extracted and applied in broader biogeographic marine contexts for marine spatial planning applications and environmental impact evaluations in marine protected areas including the Florida Keys National Marine Sanctuary.

This investigation sought to identify both typical and atypical wind patterns most directly linked to elevated light attenuation and how these patterns interact within the South Florida system. These more-resolved representations of regional circulation and associated wind patterns provide insights into precursor wind scenarios leading up to potentially harmful light attenuation events. Further, while previous water clarity studies have exploited the coupling of wave frequency, wave height, wind magnitudes, river discharge leading to sediment resuspension, and the lag-response characteristics in relation to photic depth (Fabricius, Logan, Weeks *et al.*, 2016; Chen *et al.*, 2007), such studies do not isolate specific wind patterns as precursors to “bad” water clarity conditions. The wind pattern-based methodology developed herein, when combined with other drivers, will improve predictions of water clarity events and could prove useful in understanding how the system will respond to future human-induced alterations. Lastly, since clear, healthy water is fundamental to Florida's tourism industry and to the local economies that rely on high visibility of in-water conditions (Leeworthy, Wiley and Hospital, 2004); application of these methods could also be broadened to support planning and logistics in related economic activities such as SCUBA diving, snorkeling, and recreational/commercial fishing.

## Conflict of Interest

No conflict of interest was reported by all authors.

## Acknowledgements and Funding

We thank the personnel at NASA's Goddard Space Flight Center, Ocean Biology Processing Group, for making MODIS and SeaWiFS level-2 files available and NOAA Earth System Research Laboratory, Physical Sciences Division, for providing up-to-date gridded NCEP North American Regional Reanalysis products. This research was supported by NOAA's National Center for Coastal Ocean Science and by the National Aeronautics and Space Administration's (NASA's) Research Opportunities in Space and Environmental Sciences (ROSES) funding opportunity, *Development and Testing of Potential Indicators for the National Climate Assessment*, Award NNX13AN31G.

## References

- Barnes B B, Hu C, Schaeffer B A, *et al.* (2013). MODIS-derived spatiotemporal water clarity patterns in optically shallow Florida Keys waters: A new approach to remove bottom contamination. *Remote Sensing of Environment*, 134: 377–391. <http://dx.doi.org/10.1016/j.rse.2013.03.016>.
- Barnes B B and Hu C. (2015). Cross-sensor continuity of satellite derived water clarity in the Gulf of Mexico: insights into temporal aliasing and implications for long-term water clarity assessment. *IEEE Transactions on Geoscience and Remote Sensing*, 53(4): 1761–1772. <http://dx.doi.org/10.1109/TGRS.2014.2348713>.
- Biber P D, Paerl H W, and Gallegos C L. (2005). Evaluating Indicators of Seagrass Stress to Light. In S A Bortone (Ed.), *Estuarine Indicators*. Boca Raton: CRC Press.
- Cassano E N, Gilsan J M, Cassano J J, *et al.* (2015). Self-organizing map analysis of widespread temperature extremes in Alaska and Canada. *Climate Research*, 62: 199–218. <http://dx.doi.org/10.3354/cr01274>.
- Cavazos T. (1999). Large-scale circulation anomalies conducive to extreme precipitation events and derivation of daily rainfall in northeastern Mexico and southeastern Texas. *Journal of Climate*, 12: 1506–1523. [http://dx.doi.org/10.1175/1520-0442\(1999\)012%3C1506:L SACT%3E2.0.CO;2](http://dx.doi.org/10.1175/1520-0442(1999)012%3C1506:L SACT%3E2.0.CO;2).
- Conmy R N, Coble P G, Cannizzaro J P, *et al.* (2009). Influence of extreme storm events on West Florida shelf CDOM distributions. *Journal of Geophysical Research*, 114(G4): G00F04. <http://dx.doi.org/10.1029/2009JG000981>.
- Del Castillo C E, Gilbes F, Coble P G, *et al.* (2000). On the dispersal of riverine colored dissolved organic matter over the West Florida Shelf. *Limnology and Oceanography*, 45(6): 1425–1432. <http://dx.doi.org/10.4319/lo.2000.45.6.1425>.
- Fabricius K E, Logan M, Weeks S J, *et al.* (2016). Changes in water clarity in response to river discharges on the Great Barrier Reef continental shelf: 2002–2013. *Estuarine, Coastal and Shelf Science*, vol.173: A1–A15. <http://dx.doi.org/10.1016/j.ecss.2016.03.001>
- Gramer L J. (2013). Dynamics of sea temperature variability on Florida's reef tract. *Open Access Dissertations*. Paper 1083.
- Hedley J D, Roelfsema C M, Chollett I, *et al.* (2016). Remote sensing of coral reefs for monitoring and management: A review. *Remote Sensing*, vol.8(2): 118. <http://dx.doi.org/10.3390/rs8020118>.
- Hewitson B C and Crane R G. (2002). Self-organizing maps: Applications to synoptic climatology. *Climate Research*, 22(1): 13–26. <http://dx.doi.org/10.3354/cr022013>.
- Hu C, Hackett K E, Callahan M K, *et al.* (2003). The 2002 ocean color anomaly in the Florida Bight: A cause of local coral reef decline? *Geophysical Research Letters*, 30(3): 1151. <http://dx.doi.org/10.1029/2002GL016479>.
- Hu C, Muller-Karger F E, Vargo G A, *et al.* (2004). Linkages between coastal runoff and the Florida Keys ecosystem: A study of a dark plume event. *Geophysical Research Letters*, 31(15): L15307. <http://dx.doi.org/10.1029/2004GL020382>.
- Hu C, Muller-Karger F E and Swarzenski P W. (2006). Hurricanes, submarine groundwater discharge, and Florida's red tides. *Geophysical Research Letters*, 33(11): L11601. <http://dx.doi.org/10.1029/2005GL025449>.
- Hu C, Barnes B B, Murch B, *et al.* (2014). Satellite-based virtual buoy system to monitor coastal water quality. *Optical Engineering*, 53(5): 051402. <http://dx.doi.org/10.1117/1.OE.53.5.051402>.
- Kohonen T. (1995). *Self-organizing Maps*. Vol. 30, Springer series In Information Sciences. Springer-Verlag: Berlin. pp. 362. <http://dx.doi.org/10.1007/978-3-642-97610-0>.
- Kunkel K E, Karl T R, Brooks H, *et al.* (2013). Monitoring and understanding changes in extreme storm statistics: State of knowledge. *Bulletin of the American Meteorological Society*, 94: 499–514. <http://dx.doi.org/10.1175/BAMS-D-11-00262.1>.
- Le C F, Hu C, English D, *et al.* (2013). Climate-driven chlorophyll a changes in a turbid estuary: Observation from satellites and implications for management. *Remote Sensing Environment*, 130: 11–24. <http://dx.doi.org/10.1016/j.rse.2012.11.011>.
- Lee T N, Johns E, Wilson D, *et al.* (2002). Transport processes linking south Florida coastal ecosystems. In J W Porter and K G Porter (Eds.), *The Everglades, Florida Bay, and Coral Reefs of the Florida Keys, An Ecosystem Source*

- Book. Boca Raton, FL: CRC Press. pp. 309 – 342.
- Lee Z, Darecki M, Carder K L, *et al.* (2005). Diffuse attenuation coefficient of downwelling irradiance: An evaluation of remote sensing methods. *Journal of Geophysical Research — Oceans*, 110(C2).  
<http://dx.doi.org/10.1029/2004JC002573>
- Lee Z, Lubac B, Werdell J, *et al.* (2009). An update of the quasi-analytical algorithm (QAA\_v5). Retrieved from [http://www.ioccg.org/groups/Software\\_OCA/QAA\\_v5.pdf](http://www.ioccg.org/groups/Software_OCA/QAA_v5.pdf)
- Leeworthy V R, Wiley P C and Hospital J. (2004). *Importance-satisfaction ratings five-year comparison, SPA & ER use, and socioeconomic and ecological monitoring comparison of results 1995-96 to 2000-01*. Silver Spring, MD: National Oceanic and Atmospheric Administration, National Ocean Service, Office of Management and Budget, Special Projects Division.
- Lirman D, Schopmeyer S, Manzello D, *et al.* (2011). Severe 2010 cold-water event caused unprecedented mortality to corals of the Florida Reef tract and reversed previous survivorship patterns. *PLoS ONE*, 6(8): e23047.  
<http://dx.doi.org/10.1371/journal.pone.0023047>.
- Liu Y and Weisberg R H. (2012). Seasonal variability on the West Florida Shelf. *Progress in Oceanography*, 104: 80–98.  
<http://dx.doi.org/10.1016/j.pocean.2012.06.001>.
- Lohrenz S E, Wiesenburg D A, Arnone R A, *et al.* (1999). *What controls primary production in the Gulf of Mexico?* In H Kumpf, K Steidinger, and K Sherman (Eds.), *The Gulf of Mexico Large Marine Ecosystem: Assessment*. Malden, MA: Blackwell Science, Inc. p. 151–170.
- Martinez C J, Maleski J J, and Miller M F. (2012). Trends in precipitation and temperature in Florida, USA. *Journal of Hydrology*, 452–453: 259–281.  
<http://dx.doi.org/10.1016/j.jhydrol.2012.05.066>.
- MatLab. (2015). Cluster with Self-Organizing Map with Neural Network. Retrieved from [http://www.mathworks.com/help/nnet/ug/cluster-with-self-organizing-map-neural-network.html#bss4b\\_1-3](http://www.mathworks.com/help/nnet/ug/cluster-with-self-organizing-map-neural-network.html#bss4b_1-3)
- McPherson M, Hill V J, Zimmerman R C, *et al.* (2011). The optical properties of Greater Florida Bay: Implications for seagrass abundance. *Estuaries and Coasts*, 34: 1150–1160.  
<http://dx.doi.org/10.1007/s12237-011-9411-9>.
- Mesinger F, DiMego G, Kalnay E, *et al.* (2006). North American regional reanalysis. *Bulletin of the American Meteorological Society*, vol.87: 343–360.  
<http://dx.doi.org/10.1175/BAMS-87-3-343>
- Mitchum G T and Sturges W. (1982). Wind-driven currents on the West Florida Shelf. *Journal of Physical Oceanography*, vol.12: 1310–1317.  
[http://dx.doi.org/10.1175/1520-0485\(1982\)012%3C1310:WDCOTW%3E2.0.CO;2](http://dx.doi.org/10.1175/1520-0485(1982)012%3C1310:WDCOTW%3E2.0.CO;2)
- Neely M B, Bartels E, Cannizzaro J, *et al.* (2004). *Florida's Black Water Event*. In K A Steidinger, J H Landsberg, C R Tomas, *et al.* (Eds.), *Proceedings of the International Conference on Harmful Algae*, Saint Petersburg Beach, FL, USA, 21–25 October 2002. Florida Marine Research Institute: Saint Petersburg, FL, USA. pp. 377–379.
- Obeyskera J, Park J, Irizarry-Ortiz M, *et al.* (2011). *Past and Projected Trends in Climate and Sea Level for South Florida*. Interdepartmental Climate Change Group. South Florida Water Management District, West Palm Beach, Florida, Hydrologic and Environmental Systems Modeling Technical Report. July 5, 2011.
- Palandro D, Hu C, Andréfouët S, *et al.* (2004). *Synoptic water clarity assessment in the Florida Keys using diffuse attenuation coefficient estimated from Landsat imagery*. In D G Fautin, J A Westfall, P Cartwright, *et al.* (Eds.), *Coelenterate biology 2003*. Netherlands: Springer. pp. 489–493.  
[http://dx.doi.org/10.1007/978-1-4020-2762-8\\_55](http://dx.doi.org/10.1007/978-1-4020-2762-8_55)
- Pirhalla D E, Sheridan S C, Ransibrahmanakul V, *et al.* (2015). Assessing cold-snap and mortality events in South Florida Coastal ecosystems: Development of a biological cold stress index using Satellite SST and Weather Pattern Forcing. *Estuaries and Coasts*, 38(6): 2310–2323.  
<http://dx.doi.org/10.1007/s12237-014-9918-y>.
- Ransibrahmanakul V and Stumpf R P. (2002). The use of AVHRR for estimating spatially varying critical wind stress in Florida Bay. *Journal of Coastal Research*, 18(2): 267–273.
- Roberts K, Collins J M, Paxton C H, *et al.* (2014). Weather patterns associated with green turtle hypothermic stunning events in St. Joseph Bay and Mosquito Lagoon, FL. *Physical Geography*, 35(2): 2014.  
<http://dx.doi.org/10.1080/02723646.2014.898573>.
- Sheridan S C, Pirhalla D P, Lee C C, *et al.* (2012). Evaluating linkages of weather patterns and water quality responses in South Florida using a Synoptic Climatological Approach. *Journal of Applied Meteorology and Climatology*, 52: 425–438. <http://dx.doi.org/10.1175/JAMC-D-12-0126.1>.
- Sheridan S C and Lee C C. (2011). The self-organizing map in synoptic climatological research. *Progress in Physical Geography*, 35(1): 109–119  
<http://dx.doi.org/10.1177/0309133310397582>.